RSC Advances

RSC Advances

www.rsc.org/advances

ROYAL SOCIETY OF CHEMISTRY

www.rsc.org/advances

RSC Advances

Dynamic Article Links ▶

ARTICLE TYPE

Fabrication of $Bi_2Sn_2O_7$-ZnO Heterostructures with Enhanced Photocatalytic Activity

Yonglei Xing [a], **Wenxiu Que,** [a,] * **Xingtian Yin** [a] , **Xiaobin Liu** [a], **H. M. Asif Javed** [a], **Yawei Yang** [a] and **Ling Bing Kong** [b,] *

ZnO microspheres synthesized by using a hydrolysis method were sensitized with $Bi_2Sn_2O_7$ (BSO) nanoparticles at different concentrations, which were prepared by using a hydrothermal method. Various characterization methods were employed to study microstructural, morphological, optical and
10 photocatalytic properties of the BSO-ZnO heterostructures. Effects of BSO concentration on photocatalytic activities of the as-prepared samples were also investigated. The 12.5BSO-ZnO sample exhibited the highest photocatalytic efficiency. The enhanced photocatalytic efficiency was ascribed to an effective separation of the photogenerated electrons and holes, due to the presence of the BSO-ZnO heterojunction.

15 1   Introduction

With the rapid development of industry and economy of human society over the past few decades, organic pollution has been one of the most serious environmental problems [1-3]. In order to solve these problems, semiconductor photocatalysis has been regarded
20 as one of the most ideal methods to eliminate the toxic chemicals in the environment. Also, semiconductor materials have aroused great interest in scientific area all over the world. To date, various semiconductor materials have been synthesized and studied as photocatalysts, such as metal oxides [4], sulfides [5], phosphides [6],
25 and their mixtures or solid solutions [7-10]. However, their applications under the irradiation of sunlight have been seriously impeded due to their large bandgap along with the rapid recombination of the photogenerated charge carriers [11, 12]. Hence, heterostructures and p-n junctions by coupling the wide band
30 semiconductors with other semiconductors, which have different absorption bands, such as BiOI, CdS and Bi_2O_3, have been proved to be promising candidates to overcome this drawback [13-15]. In this case, the energy levels of the composite semiconductors must match each other to form staggered heterojunction to meet
35 the requirements for practical applications.

In the field of photocatalysts, ZnO with a direct bandgap of 3.2 eV is renowned as one of the most admirable semiconductor photocatalysts due to its high photosensitivity, nontoxic nature and low cost as compared with titanium dioxide (TiO_2) [16-18].
40 However, owing to its large bandgap along with a fast recombination rate of the photogenerated electron-hole pairs, its photocatalytic activities were hindered. Therefore, various semiconductors with narrow bandgaps have been coupled with ZnO nanostructures to extend its light absorption from UV region
45 to visible region. Hence, many material systems, which include ZnO/Fe_2O_3 [18], ZnO/ZnSe [19], $CuInSe_2/ZnO$ [20], and $CuInS_2/ZnO$ [21],

have been reported and proved to be efficient photocatalysts [22, 23]. Most recently, bismuth-containing photocatalysts, such as Bi_2WO_6, $BiVO_6$ and $Bi_2O_2CO_3$ [24-26], have attracted considerable
50 attention. Similarly, $Bi_2Sn_2O_7$ (BSO) is not only a novel semiconductor with a pyrochlore structure and a bandgap of 2.86 eV, but it has also been used as a catalyst and a gas sensor [27-29]. Theoretically, the formation of a coupled semiconductor structure can efficiently improve the photocatalytic efficiency.
55   Herein, we report synthesis and characterization of BSO-ZnO heterostructures with high photocatalytic activities. Nanocrystalline BSO was synthesized by using a facile hydrothermal method, whereas ZnO microspheres were prepared through the hydrolysis of zinc salt in polyol. Two semiconductors
60 were then mixed together and annealed at 500 ℃ for 1 h so as to form the BSO-ZnO composites with a heterogeneous structure. Visible-light-mediated photocatalytic behavior of the BSO-ZnO composites for photodegradation of RhB was studied, the relationship between the composition and the photocatalytic
65 activity of the BSO-ZnO composites was systematically investigated, and the formation process and the heterogeneous structures of the BSO-ZnO composites were discussed.

2   Experimental Section

All the reactants used in this study were analytical-grade and
70 were used without any further purification treatment.

2.1   Synthesis of ZnO Microspheres

ZnO microspheres were synthesized through the hydrolysis of zinc salt as described in our previous work [30]. Typically, 0.01 mol $Zn(CH_3COO)_2 \cdot 2H_2O$ was added to 400 mL diethylene glycol
75 with constant stirring at 130 ℃ until a complete dissolution was achieved, followed by heating at 180 ℃ for 15 min. The obtained white solution was then centrifuged and rinsed with absolute

ethanol for several times to obtain high purity ZnO microspheres.

2.2 Synthesis of Bi₂Sn₂O₇ and preparation of BSO-ZnO heterostructures

Stoichiometric amounts of $K_2SnO_3 \cdot 3H_2O$ and $Bi(NO_3)_3 \cdot 5H_2O$
5 were dissolved in 10 mL dilute HNO_3 (1:10 v/v) [31]. Mixed hydroxides were then precipitated from this solution by adding $NH_3 \cdot H_2O$ till the pH value was 12. Subsequently, the mixed precipitates were transferred into a Teflon-lined stainless-steel autoclave, which was sealed and heated at 180 ℃ for 24 h.
10 Finally, the product was filtered, washed thoroughly with water and ethanol, and dried at 100℃ for 1 h.

BSO modified ZnO microspheres were prepared as follows. The as-prepared BSO powders were first dispersed in the ethanol and then mixed with the ZnO microspheres based on a required
15 molar ratio. After being thoroughly mixed through strong stirring, solid powders were thus obtained by washing and drying in air at 75 ℃, which were then directly transferred into an oven calcined at 500 ℃ for 1 h. Therefore, BSO-ZnO composite photocatalysts were obtained. Similarly, pure BSO without ZnO microspheres
20 was also prepared for comparison.

2.3 Characterization

X-ray diffraction (XRD, D/max-2200, Rigaku, Japan) with Cu Kα radiation was used to characterize phase compositions of the ZnO microspheres, the BSO-precursors and the BSO-ZnO
25 composites. Scanning electron microscopy (SEM, Quanta F250, FEI, USA) coupled with an energy-dispersive X-ray (EDX) spectrometer and transmission electron microscopy (TEM JEM-2100, JEOL Inc., Japan) were employed to observe morphological properties of the as-prepared materials. UV-Vis
30 absorption spectra of all the samples were measured by using a JASCO Model V-570 UV/VIS/NIR spectrometer equipped with a diffuse reflectance accessory. Specific surface area and average pore diameter of the nanoparticles were measured according to N_2 adsorption-desorption isotherm with an Automated Surface area
35 and Porosity Analyser. Photoluminescence spectra were recorded with a Jobin-Yvon Fluorolog-3 spectrofluorimeter at room temperature, with an excitation wavelength of 251 nm.

2.4 Photocatalytic Activity Measurement

Rhodamine B (RhB) was selected as a model pollutant to
40 evaluate photocatalytic performance of the as-prepared photocatalysts. Here, photocatalytic activities of the as-prepared samples were evaluated by observing the decomposition of the RhB aqueous solution. Typically, 35 mg photocatalyst was added to a 50 ml of RhB aqueous solution with an initial concentration
45 of 10^{-5} M in a glass reactor, which has a 115 cm² cross section and 5 cm height. The reactor was then kept in dark with continuous stirring for 0.5 h to reach the adsorption-desorption equilibrium, prior to light irradiation from a 500 W Xe arc lamp with a 420 nm cutoff filter. 5 mL of the suspension solution was
50 taken out at certain time intervals and centrifuged to remove the catalyst. Thus, the efficiency of the degradation processes was determined by monitoring the decrease in absorbance value at λ=554 nm.

3 Results and Discussion

3.1 Structural and morphological properties

Figure 1 shows XRD patterns of pure ZnO, pure BSO and the BSO-ZnO composites. It can be seen that all diffraction peaks as shown in spectra a and b can be indexed to the hexagonal phase of ZnO (JCPDS card 36-1451) and the cubic phase of BSO
60 (JCPDS card 87-0284) [27, 32]. The sharp and intense diffraction peaks of BSO and ZnO confirmed their highly crystalline nature. In addition, no impurity peaks were detected, indicating a high purity of the two components. However, for the BSO-ZnO samples, two sets of XRD peaks corresponding to ZnO and BSO
65 can be clearly observed in Figure 1 (c-h), where the peaks indicated by asterisks (*) were indexed as the cubic structure of BSO. It can be also seen that most of the peaks of the BSO-ZnO samples can be matched to those of ZnO, except three peaks assigned to the (311), (222) and (400) planes of cubic BSO, and
70 the diffraction peak intensity of BSO increased gradually as the amount of BSO was increased from 3% to 15%. The relatively higher intensity of the (222) peak in the composite samples than in the pure BSO indicated its anisotropic growth behavior and implied the preferred orientation of the crystallites.[33] However,
75 the peak intensity of ZnO decreased significantly as the BSO content was increased, suggesting that the presence of BSO inhibited the crystal growth of ZnO. In addition, the broadening of the peaks of the composite samples indicated the formation of the nanostructures in the materials [34]. Especially, the significant
80 broadening of the (002) peak of ZnO might result from the merging of the (400) plane of cubic BSO and the (002) peak of ZnO. Similarly, the same mergence was observed for the (102) peak of ZnO and the (440) peak of BSO, and the (110) peak of ZnO and the (622) peak of BSO.
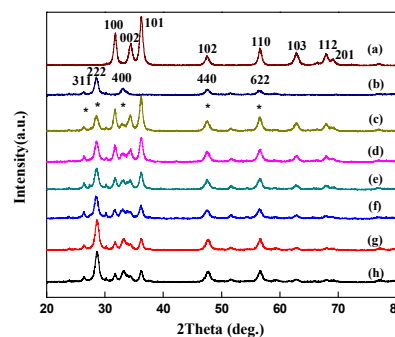
85
Fig.1 XRD patterns of pure ZnO, pure BSO, and the BSO-ZnO composites: (a) ZnO, (b) BSO, (c) 3BSO-ZnO, (d) 5BSO-ZnO, (e) 7.5BSO-ZnO, (f) 10BSO-ZnO, (g) 12.5BSO-ZnO, and (h) 15BSO-ZnO.

Figure 2 shows SEM images of pure ZnO, pure BSO and the
90 BSO-ZnO composites. It can be observed from Figure 2 (a) that the as-prepared ZnO consists of dispersive and spherical particles with smooth surface and diameter of about 200 nm. In contrast, the BSO as seen in Figure 2 (b) shows also relatively dispersive but irregular particles. However, the morphologies of the BSO-
95 ZnO composites as shown in Figures 2 (c)-(h) highly depend on the content of BSO. It can be also clearly found that some spherical nanoparticles, which have a diameter of about 20 nm, are stuck to the ZnO microspheres and the amount of these adhesive nanoparticles increase with increasing BSO content.
100 Figure 3 shows the EDX spectrum of the ZnO microspheres with

the adherent nanoparticles in the 12.5BSO-ZnO sample, which only shows O, Zn, Bi and Sn elements, implying that Bi and Sn elements are present in the adherent nanoparticles. Considering the contents of the elements as presented in **Table S1, ESI**, it can be inferred that the adherent nanoparticles should be BSO. In order to further confirm the BSO-ZnO heterostructures, TEM and HRTEM were used to investigate the detailed structure information of the BSO-ZnO composites.
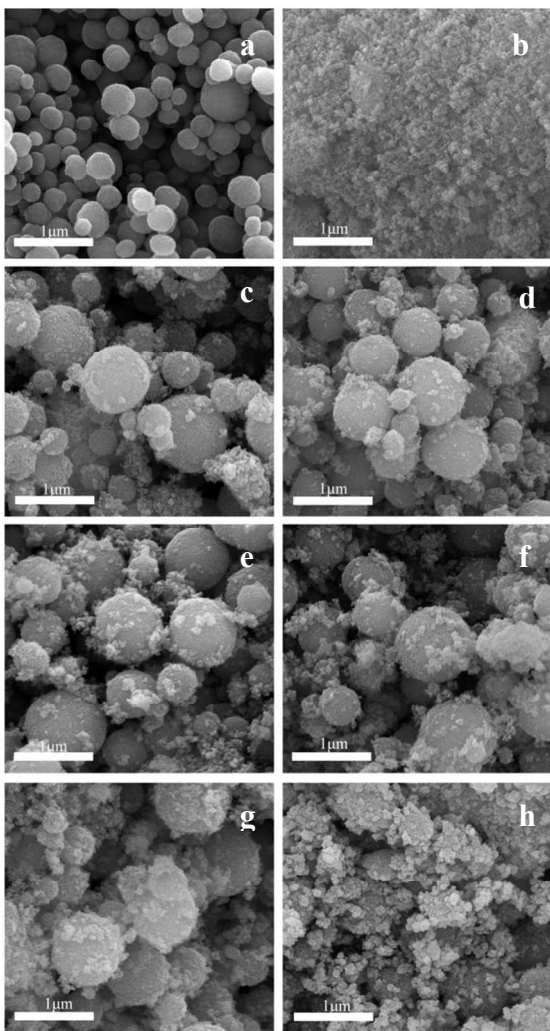
Fig.2 SEM images of (a) ZnO, (b) BSO, (c) 3BSO-ZnO, (d) 5BSO-ZnO, (e) 7.5BSO-ZnO, (f) 10BSO-ZnO, (g) 12.5BSO-ZnO and (h) 15BSO-ZnO samples.
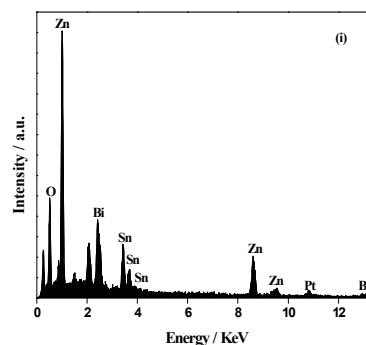
Fig.3 EDX spectrum of the 12.5BSO-ZnO sample.

Figure 4 (a) shows a typical TEM image of one microsphere in the 12.5BSO-ZnO nanocomposite sample. Obviously, the result is consistent with the SEM observation as shown in Fig. 2, in which some nanoparticles were clearly anchored on surface of the ZnO microsphere. These nanoparticles were so strongly attached to the microsphere that it is difficult to separate them during ultrosonication process. In addition, TEM images of pure ZnO and BSO are also presented in **Figure S1, ESI**. Figure 4 (b) is a HRTEM image taken within the blue square region in Figure 4 (a), revealing the highly crystalline nature of the BSO-ZnO heterostructure. Here, the well lattice fringes, with an interplanar spacings of 0.28 nm and 0.32 nm, are correspond to the (100) plane of hexagonal ZnO [35] and the (444) plane of BSO [27], respectively. These TEM results are in a good agreement with those of XRD patterns. Therefore, it can be concluded that heterojunction between the two materials has been formed.
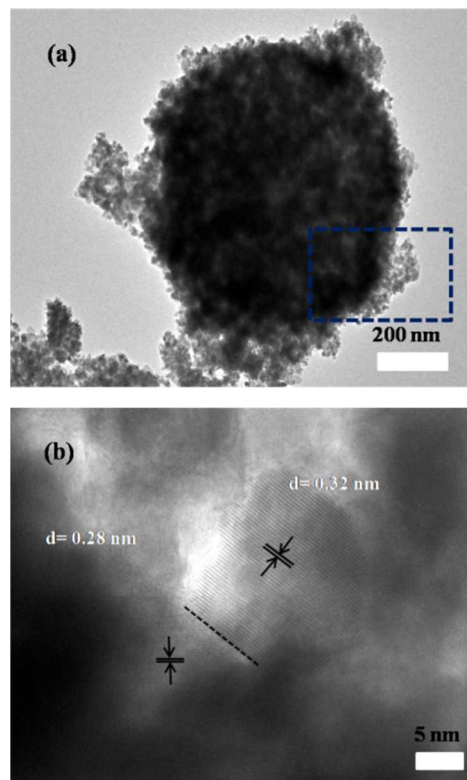
Fig.4 (a) TEM and (b) HRTEM images of the 12.5BSO-ZnO sample.

3.2 UV-Vis light absorption

UV-Vis absorption spectra of the BSO-ZnO nanocomposites with different BSO contents are shown in Figure 5 (a). For comparison, the UV-Vis absorption spectra of pure ZnO and BSO are also included. They exhibited a clear absorption edge at 380 nm and 480 nm, which belong to ultraviolet light region and visible light region, respectively. In contrast, all the BSO-ZnO nanocomposites have a pronounced absorption in the visible light and the absorbance increased gradually with increasing BSO content from 3 to 15 at%.
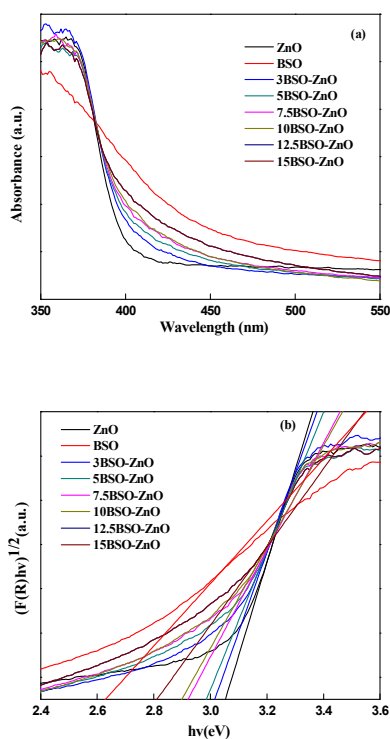
Fig.5 (a) UV-Vis diffuses reflectance spectra and (b) estimated bandgap energies of ZnO, BSO and all BSO modified ZnO samples.

Table 1 Bandgaps of all the samples.

Samples	Bandgap energies / eV
ZnO	3.05
BSO	2.62
3BSO-ZnO	3.00
5BSO-ZnO	2.98
7.5BSO-ZnO	2.92
10BSO-ZnO	2.89
12.5BSO-ZnO	2.85
15BSO-ZnO	2.80

The bandgaps of all the samples were estimated according to the following equation: [34]

$$F(R)hv = A(hv-E_g)^n \qquad (1)$$

Where $F(R)$, v, E_g and A are the absorption coefficient, light frequency, bandgap energy and the proportionality constant, respectively. The value of n describes the type of transition, with $n=1/2$ for direct transition and $n=2$ for indirect transition. All the BSO-ZnO nanocomposites have an n value of 2, which means that they have an indirect transition. [34] The bandgap energies of all these samples, which are estimated from the plot $(F(R)hv)^{1/2}$ versus hv, are shown in Figure 5 (b) and Table 1. It should be mentioned here that the value of pure ZnO is slightly smaller than that reported in the open literature, which is probably related to the quantum confinement effect in the ZnO microspheres [36]. Due to the involvement of SnO_2 in the structure of Bi_2O_3, the bandgap of pure BSO sample is 2.62 eV, which is lower than the value by 0.22 as reported in Ref. [37]. However, the bandgap energies of all the BSO-ZnO nanocomposite samples were distributed in the range of 2.8-3.01 eV. Actually, it can be also seen that the shift of their absorption edges to a longer wavelength is in an agreement with the calculated bandgap energy.

3.3 Pore size distribution and specific surface area.

Figure 6 shows N_2 absorption-desorption isotherm and pore size distribution of the 12.5BSO-ZnO sample, which displays a type-IV isotherm with a hysteresis loop according to the classification of IUPAC, indicating the presence of the mesoporous structure [38]. The formation of the mesoporous structure can be ascribed to the aggregation of the BSO nanoparticles adhering to the surface of the ZnO microspheres. The specific surface area of the sample was calculated from Figure 6b, with a value of 43.3 $m^2 \cdot g^{-1}$.
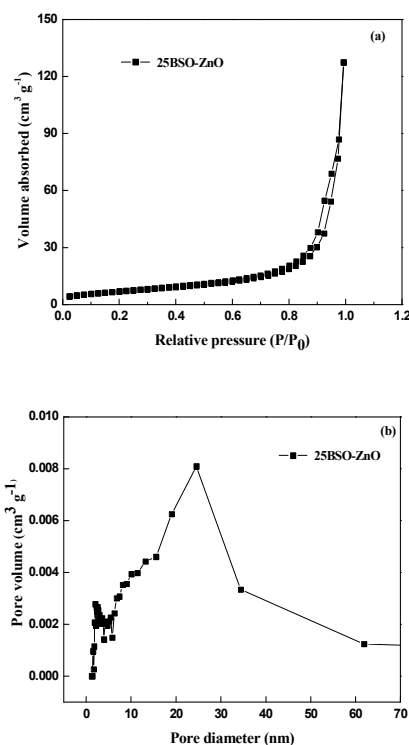
Fig.6 N_2 adsorption-desorption isotherm (a) and pore size distribution (b) of the 12.5BSO-ZnO sample.

3.4 Photocatalytic activity

Figure 7 (a) shows photocatalytic activities of all samples, including ZnO, BSO, P25 and the BSO-ZnO nanocomposites. It can be seen that ZnO, BSO and P25 show relatively lower photocatalytic activity under the simulative sunlight irradiation. The low photocatalytic activity of ZnO is due to the large bandgap (3.05 eV) and the rapid recombination of the

photogenerated charge carriers [39]. In addition, as reported by Xu *et al*, BSO can absorb visible light, but its high recombination rate still leads to low photocatalytic efficiency [27]. However, our results as seen in Figure 7 indicate that the BSO-ZnO
5 nanocomposites have much higher photocatalytic activity. Especially, the 12.5BSO-ZnO nanocomposite sample shows the best photocatalytic activity in all measured samples, which also shows better photocatalytic efficiency as compared to CTAB-$Bi_2Sn_2O_7$, nano-$Bi_2Sn_2O_7$ and $Bi_2O_3/Bi_2Sn_2O_7$ nanocomposites [27,
10 32, 37]. The photocatalytic activity of the BSO-ZnO nanocomposites increases with increasing BSO content, indicating the beneficial effect of the heterostructure on promoting photocatalytic efficiency. Besides, the first-order kinetics of RhB degradation of different samples are shown in
15 **Figure S2, ESI**. According to the first-order kinetics, the rate constants of 12.5BSO-ZnO, ZnO and BSO are calculated to be 0.011 min^{-1}, 0.0037 min^{-1} and 0.0044 min^{-1}, respectively. It is clear that the rate constant of 12.5BSO-ZnO is about 3 times and 2.5 times that of pure ZnO and BSO. Therefore, it can be
20 concluded that more electron-holes can be separated and then react with RhB molecules. However, it should be mentioned that the 15BSO-ZnO nanocomposite sample has lower activity.

To propose a reasonable photocatalytic mechanism, main active species that were responsible for the degradation of RhB
25 were also investigated. Since sodium hydrogen carbonate (NaHCO$_3$, •OH radical and h$^+$ scavenger) and disodium ethylenediaminetetraacetate (EDTA, a hole scavenger) are unstable under certain conditions, which are moderate in this experiment, they may not be used commonly. However, these
30 two scavengers are still important scavengers and have been used to probe the reactive species [40, 41]. Figure 8 shows the as-obtained result, where the photocatalytic activity was slightly depressed when EDTA (5 mM) and NaHCO$_3$ (5 mM) were added. It means that both the •OH and h$^+$ acted as main reactive species. As seen
35 in Figure 8, although the scavenging effects of EDTA and NaHCO$_3$ are not obvious, which is mainly due to the low concentrations of scavengers, the photoactivity is still suppressed more obviously by EDTA than NaHCO$_3$, indicating that h$^+$ played a more important role in promoting the RhB degradation.
40 Moreover, **Figure S3, ESI** shows first-order kinetics of RhB degradation with or without of EDTA and NaHCO$_3$. The rate constant of 12.5BSO-ZnO in RhB aqueous solution is 0.011 min^{-1}, which is 1.27 times and 1.67 times that in NaHCO$_3$ or EDTA solution.

45 Furthermore, the pH value of RhB during the degradation was also recorded, with the values shown in **Table S2**. It can be seen that, after a stirring in the dark for 1 h to establish the adsorption-desorption equilibrium, the initial pH value of the RhB was different due to a various content of the hydroxyl ions adsorbed
50 on the surface of the sample. However, on a small change of the pH value can be observed in the whole photodegradation process. It is further proved that h$^+$ had more contribution to the RhB degradation.

Photoluminescence (PL) spectra of the samples were carried
55 out to observe the separation rate of the photo-generated electron-hole pairs directly. It is well known that PL signal is derived from the recombination of the electron and hole. As shown in Figure 9, the intensity of PL peak for the 12.5BSO-ZnO sample was the

weakest, which was lower than those of pure ZnO and pure BSO
60 samples, indicating that the recombination of electron-hole pairs was effectively inhibited. Obviously, these results are consistent with the conclusion that the 12.5BSO-ZnO sample has the highest photocatalytic activity for RhB degradation.

Similar to the forming process of the ZnO/BiOI [35], the BSO
65 nanoparticles are attached to the surface of the ZnO microspheres as shown in Figure 10. Therefore, it is possible to suggest that there exists an optimized content of BSO. This is because an excess BSO content decreases the photocatalytic activity of the sample, due to a longer pathway for the migration of the
70 photogenerated charge carriers [40].
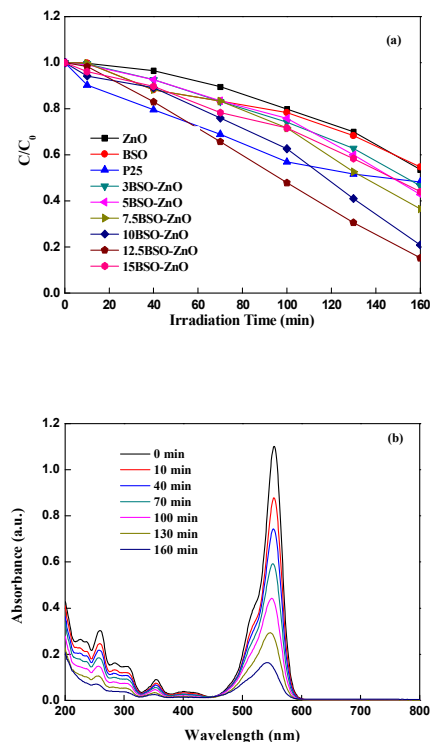
Fig.7 (a) Temporal courses of the decrease in the RhB concentration with visible-light irradiation time (b) Representative degradation profile of
75 RhB in the presence of the 12.5BSO-ZnO sample.
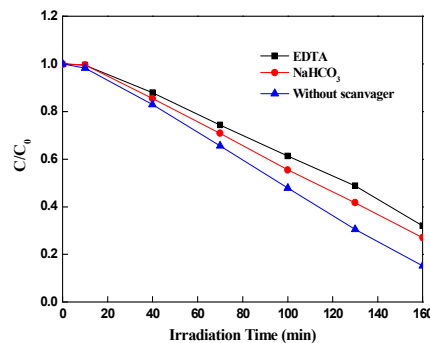
Fig.8 Photodegradations of RhB in the presence of different radical scavengers.
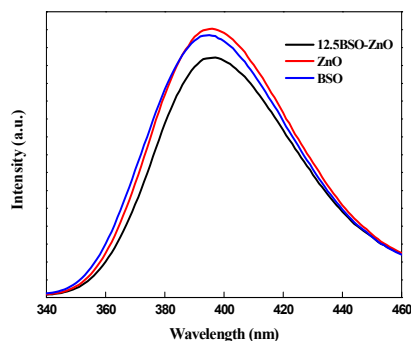
Fig.9 PL spectra of ZnO, BSO and the 12.5BSO-ZnO samples.
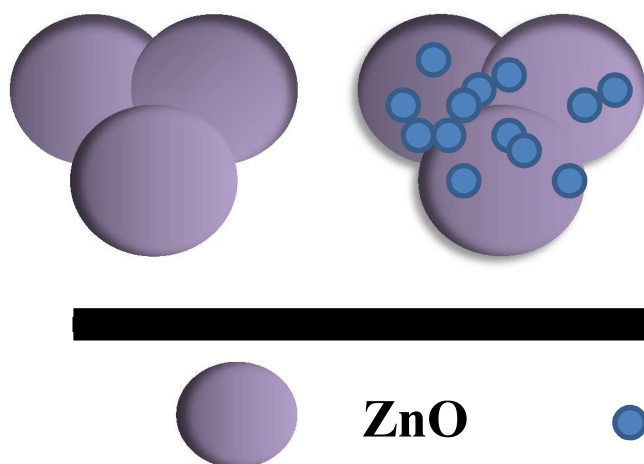
5 **Fig.10** Schematic illustration of the BSO-ZnO heterojunction system.

Based on above results, a mechanism for the formation of the heterostructure was proposed. Figure 11 (a) shows energy bands of BSO and ZnO. It is well known that ZnO is an n-type semiconductor and BSO is a p-type semiconductor, whose Fermi
10 energy level is close to the conduction band and valence band of ZnO [43, 44]. Thus, the enhanced photocatalytic activity of the BSO-ZnO nanocomposites is mainly ascribed to the presence of the heterojunciton, which inhibits the recombination of the photogenerated electron-hole pairs. Figure 11 (b) shows the
15 formation process of the heterojunction. That is, a p-n junction is formed as BSO is in contact with ZnO, so that the electrons diffuse from ZnO to BSO and the holes diffuse from BSO to ZnO, resulting in a positive section in the ZnO side and a negative section in the BSO side. When the Fermi levels of BSO and ZnO
20 reach equilibration, the charge diffusion will stop. Furthermore, the energy band of ZnO shifts downward along its Fermi level, whereas the energy band of BSO shifts upward as shown in Figure 11 (b). Hence, under an irradiation of visible light, the photogenerated electrons transfer from the conduction band of
25 BSO to ZnO, while the photogenerated holes transfer from the valence band of ZnO to BSO.
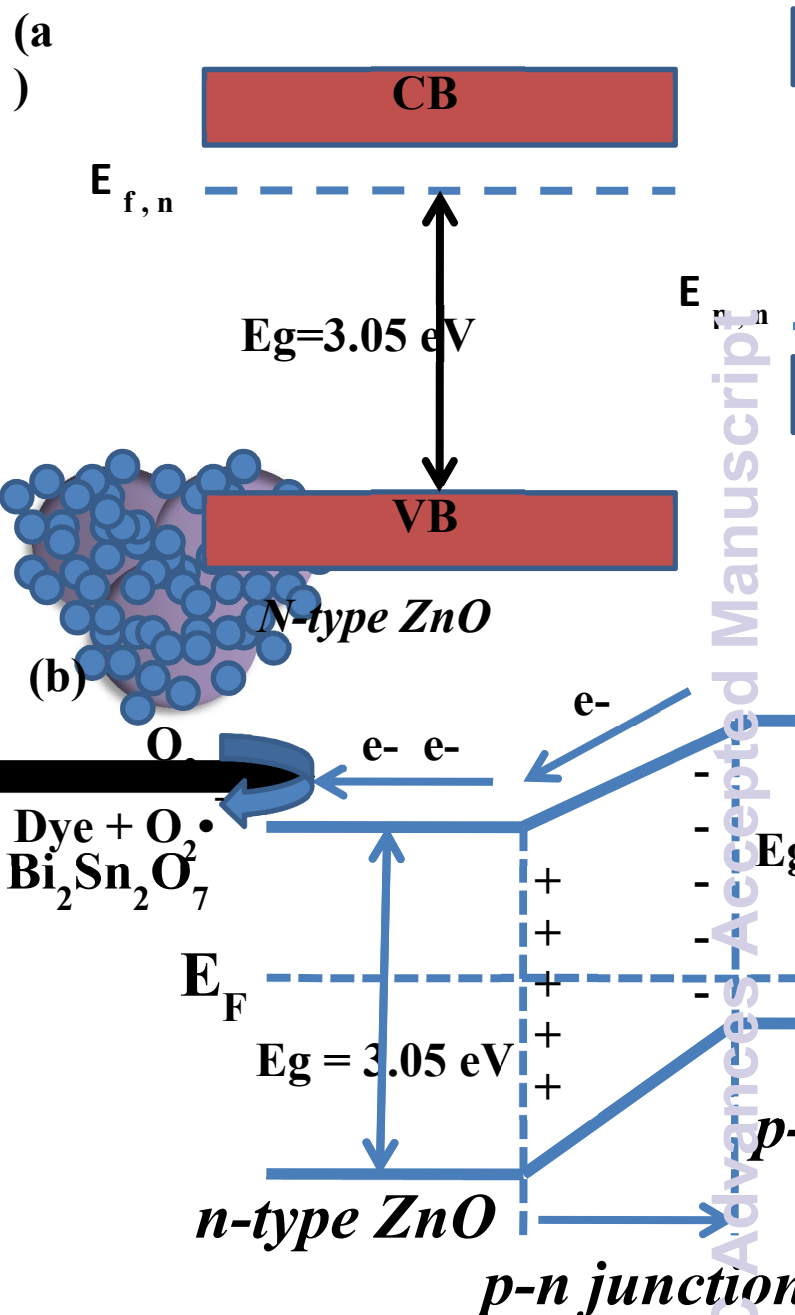
Fig.11 Diagram of (a) the bandgap of ZnO and BSO before contact, and
30 (b) the proposed electron-hole separation process of the BSO-ZnO heterojunction structure.

The photodegradation of RhB aqueous solution has been extensively studied and two possible mechanisms have been proposed [44]. It can be seen from Figure 7 (b) that the main
35 degradation process of RhB is the photodegradation under the visible light irradiation [31]. Therefore, the electrons in ZnO can react with oxygen, which is located on the surface of ZnO and acts as an electron acceptor, to form superoxide radical anion $(O_2^{\bullet-})$ [19]. Subsequently, this superoxide ion can not only react
40 with RhB molecules, but also further form hydroxyl radicals with strong oxidation ability in degrading organic molecules. Meanwhile, the holes in BSO can potentially react with water

molecules adhering to the surfaces of the BSO nanoparticles to generate hydroxyl radicals (OH•) with high reactivity. The whole electron transfer process in the degradation of the RhB aqueous solution is depicted in Figure 11 (b).

4   Conclusions

BSO-ZnO nanocomposites with a heterostructure have been synthesized by using solvothermal method and hydrolysis method. The structural, morphological, and optical properties of the BSO-ZnO nanocomposites can be controlled by regulating the content of BSO. The BSO-ZnO nanocomposites exhibited a high photocatalytic activity for the degradation of RhB in aqueous solution. The enhanced photocatalytic activity was mainly attributed to the formation of the heterojunction, which inhibited the recombination of the photogenerated electron-hole pairs. It is believed that this result is of great importance in developing new heterojunction photocatalysts for pollutant abatements.

Acknowledgements

Notes and References

[a] Electronic Materials Research Laboratory, International Center for Dielectric Research, Key Laboratory of the Ministry of Education, School of Electronic and Information Engineering, Xi'an Jiaotong University, Xi'an 710049, Shaanxi, P.R.China. *Tel.: +86-29-82668679; Fax: +86-29-82668794. Email address: wxque@mail.xjtu.edu.cn

[b] School of Materials Science and Engineering, Nanyang Technological University, Nanyang Avenue, Singapore 639798, Singapore. *Email address: elbkong@ntu.edu.sg

† Electronic Supplementary Information (ESI) available

1   Y. X. Tang, P. X. Wee, Y. K. Lai, X. P. Wang, D. G. Gong, P. D. Kanhere, T. T. Lim, Z. L. Dong and Z. Chen, *J. Phys. Chem. C*, 2012, **116**, 2772.

2   L. F. Yin, Z. Y. Shen, J. F. Niu, J. Chen and Y. P. Duan, *Environ. Sci. Technol.*, 2010, **44**, 9117.

3   S. Murcia-López, M. C. Hidalgo and J. A. Navío, *Photochem. Photobiol.*, 2013, **89**, 832.

4   C. Chen, W. M. Cai, M. C. Long, B. X. Zhou, Y. H. Wu, D. Y. Wu and Y. J. Feng, *ACS Nano*, 2010, **4**, 6425.

5   I. Zafiropoulou, M. S. Katsiotis, N. Boukos, M. A. Karakassides, S. Stephen, V. Tzitzios, M. Fardis, R. V. Vladea, S. M. Alhassan and G. Papavassiliou, *J. Phys. Chem. C*, 2013, **117**, 10135.

6   Q. X. Guan and W. Li, *J. Catal.*, 2010, **271**, 413.

7   A. B. Djurisic, X. Chen, Y. H. Leung and A. M. C. Ng, *J. Mater. Chem.*, 2012, **22**, 6526.

8   R. K. Chiang and R. T. Chiang, *Inorg. Chem.*, 2007, **46**, 369.

9   W. Ho, J. C. Yu, J. Lin, J. G. Yu and P. S. Li, *Langmuir*, 2004, **20**, 5865.

10   A. Wisitsoraat, A. Tuantranont, E. Comini, G. Sberveglieri and W. Wlodarski, *Thin Solid Films*, 2009, **517**, 2775.

11   C. Burda, Y. B. Lou, X. B. Chen, A. C. S. Samia, J. Stout and J. L. Gole, *Nano Lett.*, 2003, **3**, 1049.

12   Z. Y. Wang, B. B. Huang, Y. Dai, X. Y. Qin, X. Y. Zhang, P. Wang, H. X. Liu and J. X. Yu, *J. Phys. Chem. C*, 2009, **113**, 4612.

13   J. Cao, B. Y. Xu, B. D. Luo, H. L. Lin and S. F. Chen, *Catal. Commun.*, 2011, 13, 63.

14   G. S. Li, D. Q. Zhang and J. C. Yu, *Environ. Sci. Technol.*, 2009, 43, 7079.

15   C. Z. Li, J. Y. Zhang, J. A. Yang, T. M. Wang, X. Lv and Z. L. Tang, *Appl. Catal. A-Gen.*, 2011, 402, 80.

16   J. Bae, J. B. Han, X. M. Zhang, M. Wei, X. Duan, Y. Zhang and Z. L. Wang, *J. Phys. Chem. C*, 2009, **113**, 10379.

17   K. M. Parida, S. S. Dash and D. P. Das, *J. Colloid Interf. Sci.*, 2006, **98**, 787.

18   F. Achouri, S. Corbel, A. Aboulaich, L. Balan, A. Ghrabi, M. B. Said and R. Schneider, *J. Phys. Chem. Solids*, 2014, **75**, 1081.

19   S. Cho, J. W. Jang, J. Kim, J. S. Lee, W. Choi and K. H. Lee, *Langmuir*, 2011, **27**, 10243.

20   X. L. Wang, D. C. Pan, D. Weng, C. Y. Low, L. Rice, J. Y. Han and Y. F. Lu, *J. Phys. Chem. C*, 2010, **114**, 17293.

21   M. Y. Chiang, S. H. Chang, C. Y. Chen, F. W. Yuan and H. Y. Tuan, *J. Phys. Chem. C*, 2011, **115**, 1592.

22   Y. Liu, L. Yu, Y. Hu, C. F. Guo, F. M. Zhang and X. W. Lou, *Nanoscale*, 2012, **4**, 183.

23   C. Xu, L. X. Cao, G. Su, W. Liu, H. Liu, Y. Q. Yu and X. F. Qu, *J. Hazard. Mater.*, 2010, **176**, 807.

24   M. Shang, W. Z. Wang, L. Zhang, S. S. Sun, L. Wang and L. Zhou, *J. Phys. Chem. C*, 2009, **113**, 14727.

25   Y. Ng, A. Iwase, A. Kudo and R. Amal, *J. Phys. Chem. Lett.*, 2010, **1**, 2607.

26   F. Dong, Y. J. Sun, M. Fu, W. K. Ho, S. C. Lee and Z. B. Wu, *Langmuir,* 2012, **28**, 766.

27   W. C. Xu, Z. Liu, J. Z. Fang, G. Y. Zhou, X. T. Hong, S. X. Wu, X. M. Zhu, Y. F. Chen and C. P. Cen, Int. J. Photoenergy, 2013, **2013**, ArtID: 394079, 7 pages.

28   P. C. Andrews, P. C. Junk, I. Nuzhnaya and D. T. Thielemann, *Inorg. Chem.*, 2012, **51**, 751.

29   H. W. Kim, S. H. Shim, J. W. Lee, J. Y. Park and S. S. Kim, *Chem. Phys. Lett.*, 2008, **456**, 193.

30   J. Zhang, W. X. Que, Q. Y. Jia, P. Zhong, Y. L. Liao, X. D. Ye and Y. C. Ding, *J. Alloys Compd.* 2011, **509**, 7421.

31   F. N. Sayed, V. Grover, B. P. Mandal and A. K. Tyagi. *J. Phys. Chem. C*, 2013, **117**, 10929.

32   J. J. Wu, F. Q. Huang, X. X. Lü, P. Chen, D. Y. Wan and F. F. Xu, *J. Mater. Chem.*, 2011, **21**, 3872.

33   S. Balachandran and M. Swaminathan, *J. Phys. Chem. C*, 2012, **116**, 26306.

34   S. Martha, K. H. Reddy and K. M. Parida. *J. Mater. Chem. A*, 2014, **2**, 3621.

35   J. Jiang, X. Zhang, P. B. Sun and L. Z. Zhang. *J. Phys. Chem. C,* 2011, **115**, 20555.

36   G. K. Zhang, X. Shen and Y. Q. Yang, *J. Phys. Chem. C*, 2011, **115**, 7145.

37   M. M. Mohamed and S.A. Ahmed, *Micropor. Mesopor. Mater.*, 2015, **204**, 62.

38   J. G. Yu, L. J. Zhang, B. Cheng and Y. R. Su, *J. Phys. Chem. C*, 2007, **111**, 10582.

39   F. Y. Shen, W. X. Que, Y. C. He, Y. Yuan, X. T. Yin and G. F. Wang, ACS Appl. Mater. Inter., 2012, **4**, 4087.

40   F. F. Duo, Y. W. Wang, X. M. Mao, C. M. Fan and H. Zhang, *Cryst. Res. Technol.*, 2014, **49**, 721.

41   J. Fu, Y. L. Tian, B. B. Chang, F. N. Xi and X. P. Dong, *J. Mater. Chem.,* 2012, **22**, 21159.

42   Y. L. Tian, B. B. Chang, Z. C. Yang, B. C. Zhou, F. N. Xi and X. P. Dong, *RSC Adv.*, 2014, **4**, 4187.

43   Q. F. Tian, J. D. Zhuang, J. X. Wang, L. Y. Xie and P. Liu, *Appl. Catal. A-Gen.*, 2012, **425**, 74.

44   T. X. Wu, G. M. Liu and J. C. Zhao, *J. Phys. Chem. B*, 1998, **102**, 5845.